



# Effect of heat treatments on microstructure and mechanical properties of AlSi10Mg alloys fabricated by laser powder bed fusion

Xiaogang Zhu<sup>1,2,3</sup> · Dafan Du<sup>1</sup> · Anping Dong<sup>1</sup> · Qinyao Sun<sup>1</sup> · Jing Sun<sup>2</sup> · Lijie Guo<sup>2</sup> · Baode Sun<sup>1</sup> · Zhendong Chen<sup>4</sup>

Received: 7 December 2022 / Accepted: 17 June 2023 / Published online: 24 June 2023  
© The Author(s), under exclusive licence to Springer-Verlag London Ltd., part of Springer Nature 2023

## Abstract

This study investigated the microstructures and tensile properties of as-build and heat-treated (including T6, T2, and T6-T2 treatments) AlSi10Mg samples fabricated by laser powder bed fusion (LPBF). The microstructure analysis revealed that the trend of eutectic Al-Si phase distribution along grain boundaries for heat-treated samples was significantly weakened, and the eutectic Al-Si phase was transformed into Si particles which were uniformly distributed in  $\alpha$ -Al matrix. For the T6-T2-treated specimens, the Si content in particles was the highest. Meanwhile, the T6 treatment increased the proportion of equiaxed grains on vertical section most significantly. However, in the wake of heat treatments, the average grain size on horizontal section had little change while the average grain size on vertical section was increased. The properties analysis demonstrated that the T6-T2-treated specimens obtained the best elongation and worst strength. Besides, the T6 treatment eliminated the anisotropy of the LPBFed specimens basically and synergistically obtained the best combination of strength and plasticity. The T6 treatment weakened the direction difference to the greatest extent, whereas the T2 treatment minimized the stress concentration. According to the comparative finding, the Si content in particles played an important part in properties. Besides, the relationship among inverse pole figure (IPF) maps, pole figure (PF) maps, the mass fraction and distribution of Si in Al matrix and Si particle, the grain size, kernel average misorientation (KAM), and mechanical properties under different heat treatments was established, which provided a new idea for the selection of heat treatments on LPBFed parts.

**Keywords** Laser powder bed fusion · AlSi10Mg · Microstructure · Mechanical properties · Heat treatment

## 1 Introduction

With the development of the additive manufacturing (AM), more and more types of AM processes have been developed to manufacture complex products [1]. Laser powder

bed fusion (LPBF), as one of the most important additive manufacturing methods, has been widely applied in various industries, such as aerospace and aviation. Meanwhile, AlSi10Mg is one of the most researched aluminum alloys by LPBF due to its high strength and light weight. Beyond that, there is a high manufacturing cost as well as low possibility of realizing innovative design by traditional manufactured AlSi10Mg [2, 5]. Apart from that, Calignano et al. analyzed the effect of the manufacturing strategy in the construction of thin walls in AlSi10Mg alloy, which showed that it is possible to obtain well-defined thin walls by appropriate LPBF strategies [6]. Yang et al. found that the surface roughness of the vertical section was improved by optimized process parameters for the LPBFed AlSi10Mg specimens [7]. However, one of the main challenges for application is how to improve the microstructures and properties of the LPBFed AlSi10Mg specimens by heat treatments.

Recently, it has been widely reported about the impact of heat treatments on the microstructures, properties, corrosion behaviors, and aging behaviors of various aluminum alloys

✉ Dafan Du  
dafand@sjtu.edu.cn

✉ Anping Dong  
apdong@sjtu.edu.cn

<sup>1</sup> Shanghai Key Lab of Advanced High-temperature Materials and Precision Forming and State Key Lab of Metal Matrix Composites, School of Materials Science and Engineering, Shanghai Jiao Tong University, Shanghai 200240, China

<sup>2</sup> Shanghai Aerospace Equipment Manufacturer Limited Company, Shanghai 200245, China

<sup>3</sup> Taier (Anhui) Industrial Technology Service Co., Ltd, Maanshan 243000, China

<sup>4</sup> Jiangsu Yongnian Laser Forming Technology Co., Ltd, Suqian 223800, China

fabricated by LPBF. Shen et al. [8] investigated the effect of heat treatments on the microstructures and mechanical properties of Al-Mg-Sc-Zr alloy fabricated by LPBF. As indicated by the results, the rapid aging treatment at 330 °C for 1 h could obtain a good combination of strength and plasticity, with a tensile strength of 479 MPa, a yield strength of 441 MPa, and a percentage elongation after break of 14.5%. As pointed by Wang et al. [9], upon solution treatment with aging, the yield strength of the LPBFed Al-Cu-Mg-Zr alloy reached 402 MPa, which was higher than the as-fabricated samples with the yield strength of 376 MPa. Through the artificial aging treatment, the Al-Zn-Mg alloy could be strengthened by the formation of precipitates rich in Mg and Zn as studied by Babu et al. [10]. In addition, Xiao et al. [11] explored the effect of T6 heat treatment on the microstructures and mechanical properties of LPBFed TiB<sub>2</sub>/Al-7Si-Cu-Mg alloy. It was found that there was a 16% decrease of yield strength caused by the breaking of fine microstructure. Owing to the annealing treatment or solution heat treatment, the evaluation of the microstructures could be controlled, and the properties of the Al-12Si LPBF samples could also be turned [12, 13]. In the wake of T6 heat treatment, the hardness of the LPBF Al-Zn-Mg-Cu alloy samples increased from  $133 \pm 6 \text{ HV}_{0.05}$  to  $219 \pm 4 \text{ HV}_{0.05}$ , and almost all the  $\eta$  particles were dissolved in the Al-matrix [14]. During the heat treatment at 300 °C, the stress level of the LPBFed Al-50Si alloy samples was homogenized without changing the microstructures. In addition, the average values of the residual stress decreased, while the grain size increased at higher temperatures [15]. Apart from that, the compressive yield strength of the LPBF TiB<sub>2</sub>/Al-Cu-Mg-Si specimens was improved by the grain refinement owing to the heat treatment [16]. If followed by the heat treatment at 1000 °C, the LPBFed AlCoCuFeNi high-entropy alloy (HEA) samples had the better compressive fracture strength of 1600 MPa, a yield strength of 744 MPa, and a strain of 13.1% [17]. Compared with the heat-treated specimens, the LPBFed Al-Mg-Sc-Zr specimens had a superior corrosion resistance [18].

It is worth mentioning that more studies are focused on the LPBFed AlSi10Mg alloy followed by different heat treatments. As reported by Wang et al. [19], a small amount of Si phase for AlSi10Mg specimens was precipitated in the  $\alpha$ -Al matrix by the heat treatment of solid solution. Furthermore, the fusion and enrichment of eutectic Si led to  $\alpha$ -Al matrix softening and reduction in strength. As pointed out by Wei et al. [20], the T6 heat treatment rejected Si from supersaturated  $\alpha$ -Al matrix, in order to form Si particles. At the same time, the Si-rich cellular boundaries of the LPBFed AlSi10Mg samples were transformed into Si particles, and the Mg<sub>2</sub>Si particles were also formed. Based on the T6 heat treatment, the mechanical properties of the AlSi10Mg samples were influenced by the size and number of Si particles. Besides,

the tensile strength decreased from  $434.257 \pm 10.7$  to  $168.11 \pm 2.4$  MPa. In contrast, the fracture strain increased from  $5.3 \pm 0.22$  to  $23.7 \pm 0.84\%$  [21]. Moreover, the solid treatment at 530 °C for 6 h could reduce the direction difference of the tensile properties of the LPBFed AlSi10Mg specimens [22]. The properties of the LPBFed AlSi10Mg samples were similar to those of T5 treatment samples, yet better than T6 treatments [23]. The thermal conductivity of the LPBFed AlSi10Mg samples, followed by an anneal heat treatment post-processing step, increased by 18–41% [24].

Apart from that, the values of KAM for the LPBFed AlCoCrFeNi<sub>2.1</sub> samples marked as rainbow vary from 0 to 5° attributed to the deformation inhomogeneity [25]. The value of KAM was closely related to the defects such as crack, and the value of KAM around the crack was higher than other areas [26]. In general, the smaller the value of KAM, the lower the degree of plastic deformation [27]. Therefore, the KAM is crucial for revealing the deformation mode and mechanism in metals.

In order to support improving the microstructures and properties of the LPBFed AlSi10Mg samples, it is necessary to systematically study the effect of heat treatments (T6, T2, and T6-T2) on microstructure and mechanical properties of AlSi10Mg alloy fabricated by LPBF. Therefore, a series of experiments had been conducted in this research to investigate the microstructures and tensile properties of LPBFed and heat-treated samples and explore appropriate heat treatment method to control the evaluation of the microstructure and obtain different combinations between strength and plasticity.

## 2 Experimental procedures

### 2.1 Powder material

In this study, gas-atomized AlSi10Mg powder with the size of 20–63  $\mu\text{m}$  was used as the raw material. As illustrated in Fig. 1, the particle morphology is almost worm-like. The chemical composition of AlSi10Mg alloy powder is shown in Table 1.

### 2.2 Experiment methods

All the samples were produced by Kre-AM350 in Fig. 2a, and the process parameters were constant laser power (P) of 400 W, scanning speed (v) of 930 mm/s, hatch spacing (h) of 0.07 mm, layer thickness (t) of 0.025 mm, and scanning strategy of chessboard, as shown in Fig. 2b. Furthermore, the cross-sectional area of specimens was divided into black and white chessboards. Firstly, the powder in the black chessboard was melted by the laser. Then, the powder in the white chessboard was melted. The interlayer rotation angle was 67°, and the size of chessboard was 5 mm. Besides, the

**Fig. 1** SEM images of AISi10Mg alloy powder. **a** Low magnified. **b** High magnified

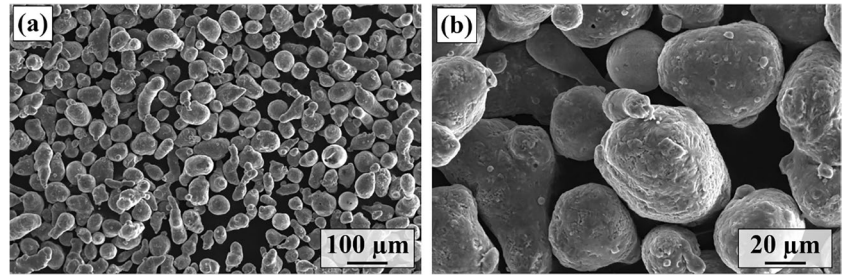
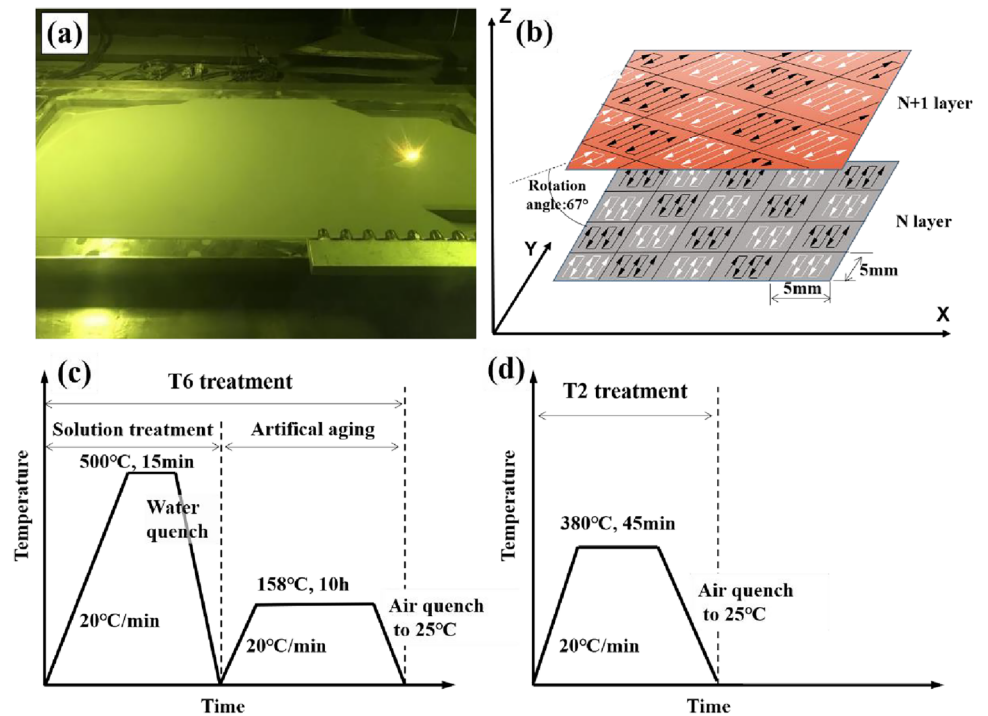


**Table 1** Chemical composition of AISi10Mg alloy powder (mass) %

Al	Si	Mg	Fe	N	O	Ti	Zn	Mn	Ni	Cu	Pb	Sn
Bal.	9.94	0.27	0.15	0.004	0.12	0.009	0.004	0.002	0.003	0.004	<0.002	<0.02

**Fig. 2** Details of the LPBF experiments. **a** LPBF process. **b** Laser scanning strategy. **c** Schematic of T6 heat treatment procedures. **d** Schematic of T2 heat treatment procedures



substrate was preheated to 80 °C, and the oxygen concentration of the build chamber was less than 1000 ppm by filling the build chamber with argon. In addition, the heat treatment procedures including T6 and T2 are displayed in Fig. 2c, d.

In order to study the impact of heat treatment on microstructures and tensile properties of AISi10Mg, specimens were subject to three kinds of heat treatment strategies (see Table 2) and compared with the LPBFed specimens.

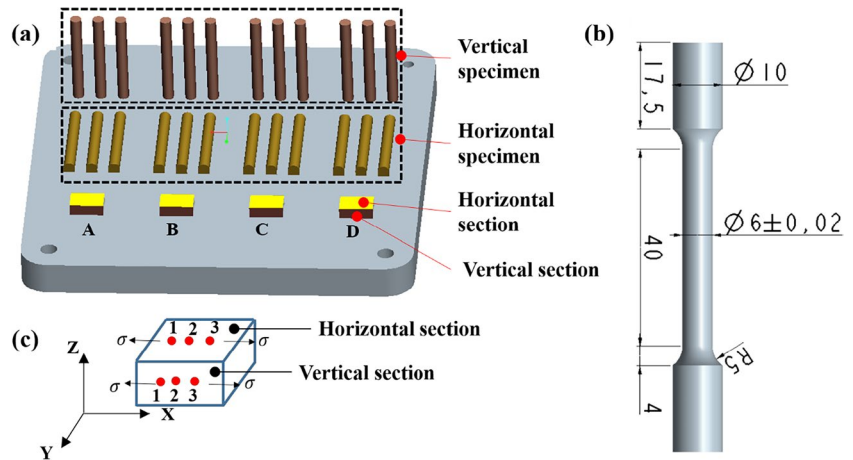
Tensile properties and microstructure specimens were fabricated by LPBF and taken from the substrate by wire cutting, as shown in Fig. 3a, and divided into “horizontal” and “vertical.” According to the GB/T 228-2002, the tensile specimens were made into standard specimens referring to Fig. 3b, and the tensile tests were conducted on universal testing machine called CMT5305. Beyond that, every

**Table 2** Utilized heat treatment parameters of LPBFed AISi10Mg

Specimen number	Heat treatment number	T6 treatment	T2 treatment
A	HT1	/	/
B	HT2	T6	/
C	HT3	/	T2
D	HT4	T6	T2

kind of specimen was measured for three times to obtain the average value. The microstructures and morphologies of the LPBFed specimens were observed by optical microscope (OM), a scanning electric microscope (SEMNOVA NANOSEM450) equipped with an electron back-scattered

**Fig. 3** **a** Schematic position of tensile specimens and micro-structure specimens. **b** Dimension of tensile specimens. **c** Test point distribution of residual stress



diffraction system (EBSD) and an energy dispersive spectrometer (EDS). The LPBFed specimens were placed on the platform of X diffractometer called TEC 4000. Besides, the X-ray emitted by the X-ray tube was used to examine the residual stress of the test points identified in Fig. 3c.

### 3 Results and discussion

#### 3.1 Microstructure

Figure 4 shows the typical morphologies of the LPBFed AlSi10Mg specimens, including “horizontal section” and “vertical section.” For the “horizontal section,” the distribution of the molten pools was tightly arranged, which was consistent with the chessboard scanning. Besides, the width of the molten pools was about  $138\ \mu\text{m}$ , and the shape of molten pools was oval in Fig. 4a. In addition, the light-color precipitates were distributed at the molten pool boundaries. For the “vertical section,” the molten pools were crescent-shaped in Fig. 4b. Apart from that, the molten pools are related to the powder or the solidified part, resulting in the high cooling rates at layer-to-layer transition regions. Therefore, there were obvious differences of microstructures for the LPBFed AlSi10Mg samples that were caused by the LPBF principle and the chessboard scanning.

**Fig. 4** Typical morphologies of the LPBFed AlSi10Mg specimens. **a** Horizontal section. **b** Vertical section

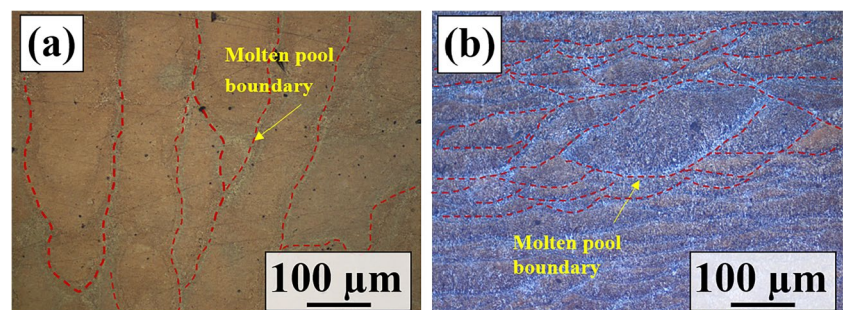
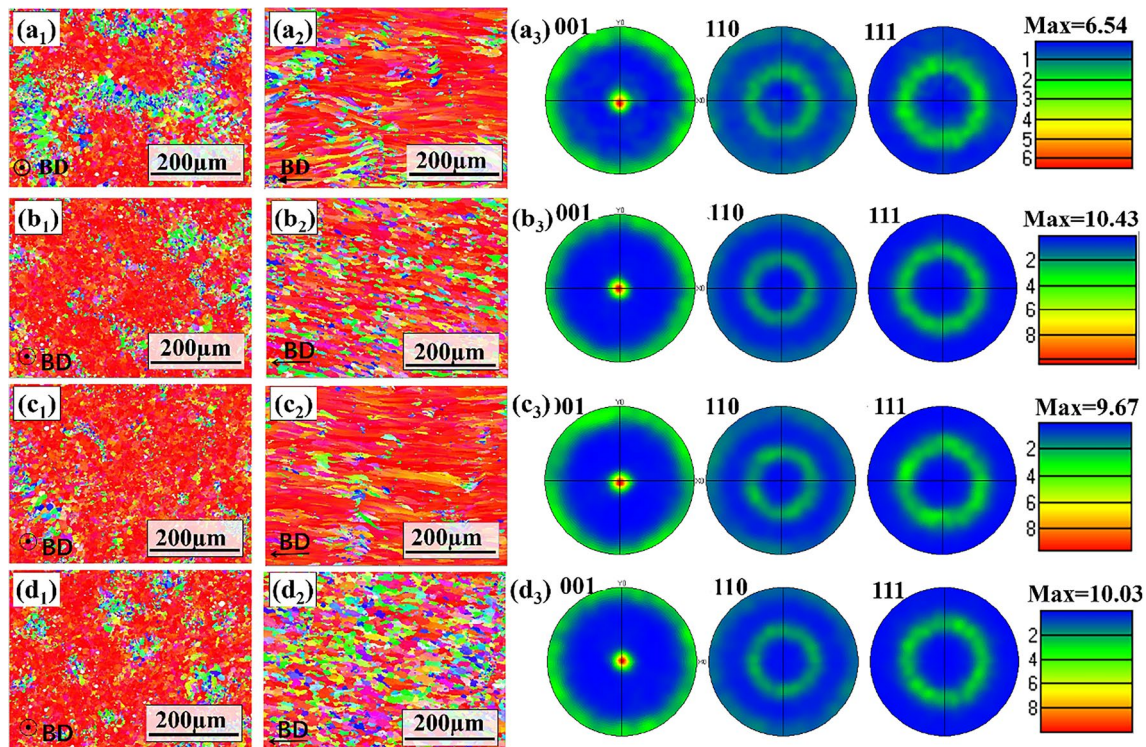


Figure 5 shows the inverse pole figure (IPF) maps on horizontal section, IPF maps on vertical section, and pole figure (PF) maps on the horizontal section under different conditions including as-printed, T6 treatment, T2 treatment, and T6-T2 treatment. Figure 6 shows the grain size distribution histograms on horizontal section and vertical section under different conditions including as-printed, T6 treatment, T2 treatment, and T6-T2 treatment. It can be observed from Fig. 5 that the as-printed AlSi10Mg specimen on vertical section presented a typical columnar grain structure on vertical section and a strong  $\langle 001 \rangle$  texture. However, the as-printed AlSi10Mg specimen on horizontal section mainly consisted of equiaxed grains. By comparing Fig. 5a and Fig. 5c, it can be found that the T2 sample on vertical section remained  $\langle 001 \rangle$  texture parallel to the building direction, but the average grain size became larger. After the heat treatments, the average grain size on horizontal section had little change as shown in Fig. 6. The formation of equiaxed grains would interrupt the growth of the columnar grains resulting in decreasing the length of some of columnar grains. Besides, the intensity of the  $\langle 001 \rangle$  fibre texture was increased after heat treatments, as the maximum pole-density projection values of  $\{001\}$  plane were larger than those of the as-printed sample, as shown from Fig. 5, which was different from the result of the LPBFed AlSi10Mg specimens after T6 heat treatment



**Fig. 5** IPF maps on horizontal section, IPF maps on vertical section, and pole figure (PF) maps on the horizontal section under different conditions. **a** As-printed. **b** T6 treatment. **c** T2 treatment. **d** T6-T2 treatment

[21]. Notably, the proportion of equiaxed grains on vertical section increased, which was favorable to reduce anisotropy degree of the mechanical properties.

Figure 7 illustrates the microstructures, including “horizontal section” and “vertical section” after different heat-treated conditions. The heat treatment could significantly affect the difference of microstructure between “horizontal section” and “vertical section.” Moreover, to reveal the effect of the heat treatment on the element distribution, Fig. 8 displays the spot EDS measurements of the “horizontal section” specimens and comparison of Si content in Si particle and Al matrix.

For the as-build specimens, according to the Al-Si binary phase diagram [21, 22], the solidification pathway of the LPBFed AlSi10Mg has experienced a crystallization reaction  $L \rightarrow L + \alpha(\alpha\text{-Al matrix})$  and a eutectic reaction  $L \rightarrow \alpha(\alpha\text{-Al matrix}) + \beta$  (eutectic Al-Si phase) at 577 °C. The primary  $\alpha$ -Al matrix was first generated (see Fig. 7a). Apart from that, the eutectic Al-Si phase was generated and distributed along the molten pool boundaries with the decrease of temperature. Besides, the microstructure at the center of the molten pools performed typical cellular dendrite structure. The existence of the dark area was resulted from the generation of the  $\alpha$ -Al matrix, in which the mass of Si was about 10.26%, as shown in Fig. 8. However, the mass of Si in the white bands increased to 14.64% and generated as the

eutectic Al-Si phase. Additionally, there was little difference between the content of Mg element in the grain and the grain boundary, indicating that Mg has no segregation tendency and is evenly distributed in the matrix.

As expressed by Wei et al. [20], the sequence of precipitation of the LPBFed AlSi10Mg specimens during heat treatment was AlSSS (supersaturated solid solution)  $\rightarrow$  aggregation of Si/ Mg atoms (GP zones)  $\rightarrow$  dissolution of Mg  $\rightarrow$  formation of Si/Mg atoms cluster  $\rightarrow$  a small number of unknown phases  $\rightarrow$  precipitation of  $\beta'$  phase  $\rightarrow$  precipitations of  $\beta'$  and  $\beta''$  phases  $\rightarrow$  stable precipitation of Si particles.

Apart from that, Rao et al. [28] found that the network Si phase of A357 alloy had disappeared, after holding at 535 °C for 15 min with the extension of time, and the Si begin to gather and grow. Besides, the size of Si particles was the largest at 24 h. However, as the holding time continued to increase, the Si particles in  $\alpha$ -Al matrix no longer continued to grow.

The process of partial dissolution, fracture, and passivation of eutectic Al-Si phase could be explained by the Gibbs-Thomson effect, expressed as follows:

$$\ln \frac{C_R}{C(\infty)} = \frac{2\sigma V_m}{RT_r} \quad (1)$$

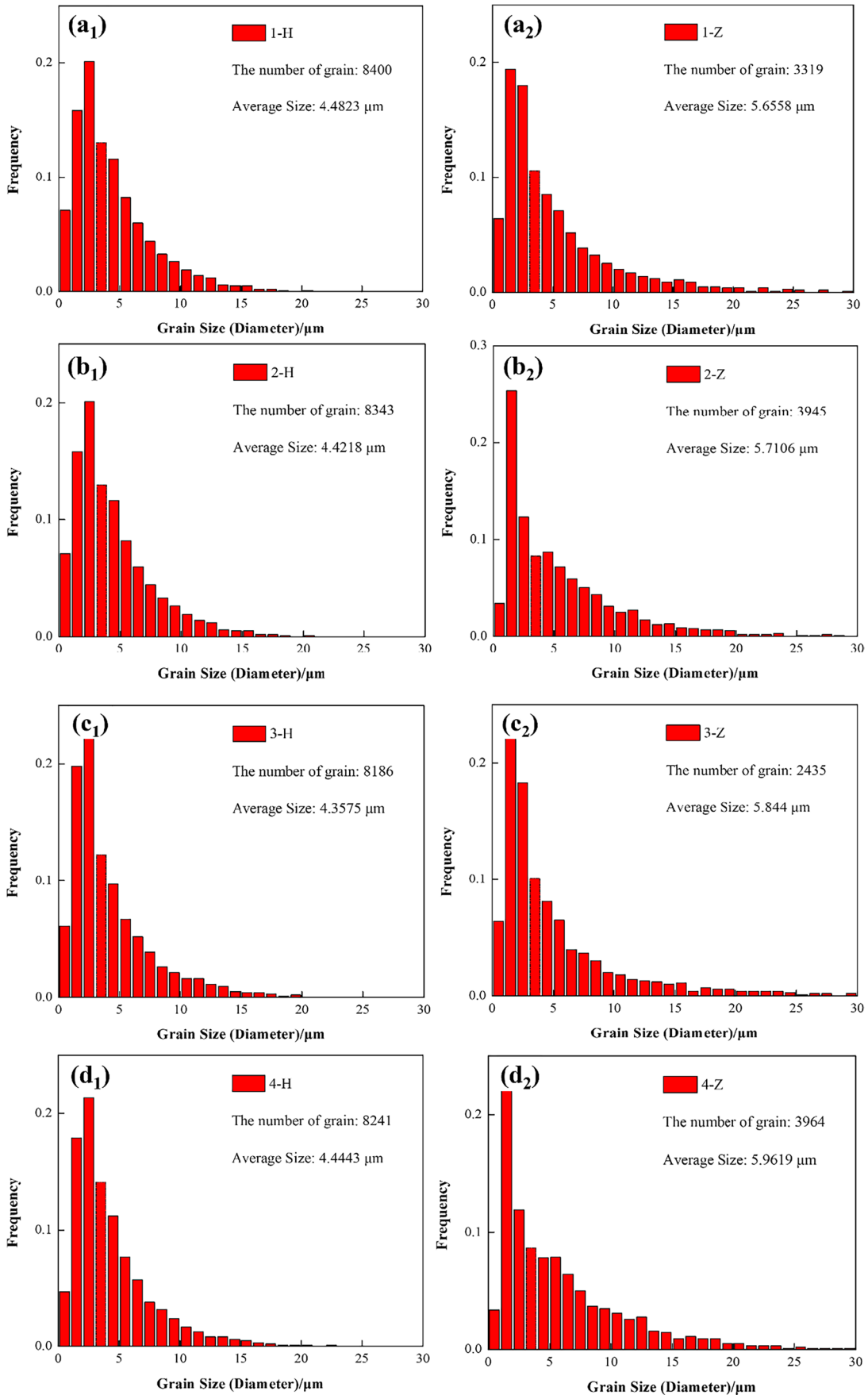


**Fig. 6** Grain size distribution histograms on horizontal section and vertical section under different conditions. **a** As-printed. **b** T6 treatment. **c** T2 treatment. **d** T6-T2 treatment

where  $C$  represents the solubility of the solute,  $r$  represents the radius of the particle,  $\sigma$  represents the surface tension on the particle boundary,  $V_m$  represents molar volume,  $R$  represents the molar gas constant, and  $T$  represents the thermodynamic temperature.

The increment of free energy of the particle is expressed as follows:

$$\Delta p = 2\sigma/r \quad (2)$$

where  $\sigma$  represents the surface tension on the particle boundary and  $r$  represents the radius of the eutectic Al-Si phase.

According to Formulas 1 and 2, it is found that the smaller the radius of the eutectic Al-Si phase is, the greater the curvature is, the greater the free energy is, and the easier the diffusion is. So, the grooves or corners of eutectic Al-Si phase are easy to diffuse and dissolve, and the corners of eutectic Al-Si phase are passivated to make the outer surface of dendrites smooth in the dissolution process.

The T6 treatment transformed the eutectic Al-Si phase into Si particles uniformly distributed in  $\alpha$ -Al matrix as shown in Fig. 7b. Beyond that, the atomic distortion of supersaturated solid solution of the eutectic Al-Si phase called  $\beta'$  phase or  $\beta''$  phase generated by solution treatment might result in large residual stress and hinder the movement of dislocations, where would store high distortion energy. Moreover, the  $\beta'$  phase and  $\beta''$  phase in an unstable state would form the new phases easily, in order to reduce distortion energy. Thus, during the T6 treatment process, the eutectic Al-Si phase was finally transformed into Si particles after first fused and then spheroidized. Besides, the mass fraction of Si in the particles could reach 31.48 wt%, whereas the mass fraction of Si in the Al matrix was about 9.41 wt% in Fig. 8.

During the T2 treatment process, the Si particles had enough time to precipitate under the condition of high temperature. As shown in Fig. 7c, the morphology of Si particles was small and spherical. The size of Si particles spheroidized decreases to nanoscale. Moreover, the Si particles were fully refined and evenly distributed in the Al matrix. Meanwhile, the mass fraction of Si in the particles could reach 35.93 wt%, while the mass fraction of Si in the Al matrix was about 10.08 wt%, as displayed in Fig. 8.

For the samples treated by the T6-T2 treatment, the spherical Si and flake Si were distributed in the Al matrix in Fig. 7d. According to the XRD results, the contents of Si in the particles and the Al matrix were completely different. To be specific, the mass fraction of Si in the particles

reaches 51.68 wt%, whereas the mass fraction of Si in the Al matrix was about 6.92 wt% in Fig. 8. Compared with the LPBFed samples, the trend of Si distribution along the molten pool boundary was significantly weakened after the heat treatments. Besides, the color of Si particles became shallower, and the mass fraction of Si in the particles was the largest by T6-T2 treatment than the other heat treatments as shown Fig. 8, indicating that the Si element experienced the whole process of “fully diffusion - nucleation-precipitation - growth” and reached a stable state finally.

### 3.2 Mechanical properties

The obvious differences in the mechanical properties and residual stress of the LPBFed AlSi10Mg under different conditions are determined by the evaluation of the microstructure, as shown in Fig. 9, Table 3, and Table 4. Obviously, the mechanical properties of the horizontal direction were better than those of the vertical direction, due to the distribution of the microstructure in layers and the weaker bounding force between the layers in Fig. 4. However, the LPBFed AlSi10Mg specimens were easy to form the Al-supersaturated solid solution, due to the fast-cooling rate in the LPBF process. The mechanism of solid solution strengthen was good for improving the strength of the LPBFed AlSi10Mg specimens, but the disadvantage was poor plasticity.

Furthermore, the heat treatments play an important part in improving the plasticity at the expense of strength. Rao et al.'s study [28] suggested that the strength of LPBFed A357 alloy decreased, and the plasticity increased after T6 treatment. Besides, Han et al. [29] found that the yield strength of the LPBFed AlSi10Mg specimens was reduced from 200 to 100 MPa while the elongation increased from 6 to 22%, after solution-treated at 550 °C for 2 h. In comparison to the LPBFed AlSi10Mg samples, the strength of the T2 treatment samples reduced by over 50%, while the elongation was twice as large as the LPBFed samples. For the T6-T2 treatment, the strength was further reduced, and the plasticity was also increased, related to the formation of Si particles as shown in Fig. 7. After the T6-T2 treatment, the network-like Mg<sub>2</sub>Si particles were dissolved and broken to grow the finely disappeared Si particles resulting in weakening the effect of hindering the motion of the dislocation, which would increase the plasticity. However, the splitting effect of the finely disappeared Si particles on the  $\alpha$ -Al matrix increased, which would decrease the strength.

In contrast, the properties of vertical specimens by T6 treatment were a tensile strength of 292 MPa, a yield strength of 245 MPa, and a percentage elongation after the break of 11.8%. Furthermore, the properties of horizontal specimens were a tensile strength of 298 MPa, a yield strength of 250 MPa, and a percentage elongation after the break of 13.1%.

**Fig. 7** SEM images of AlSi10Mg samples LPBFed under different conditions. **a** As-build. **b** T6. **c** T2. **d** T6-T2. (“1” represents “Horizontal”; “2” represents “Vertical”)

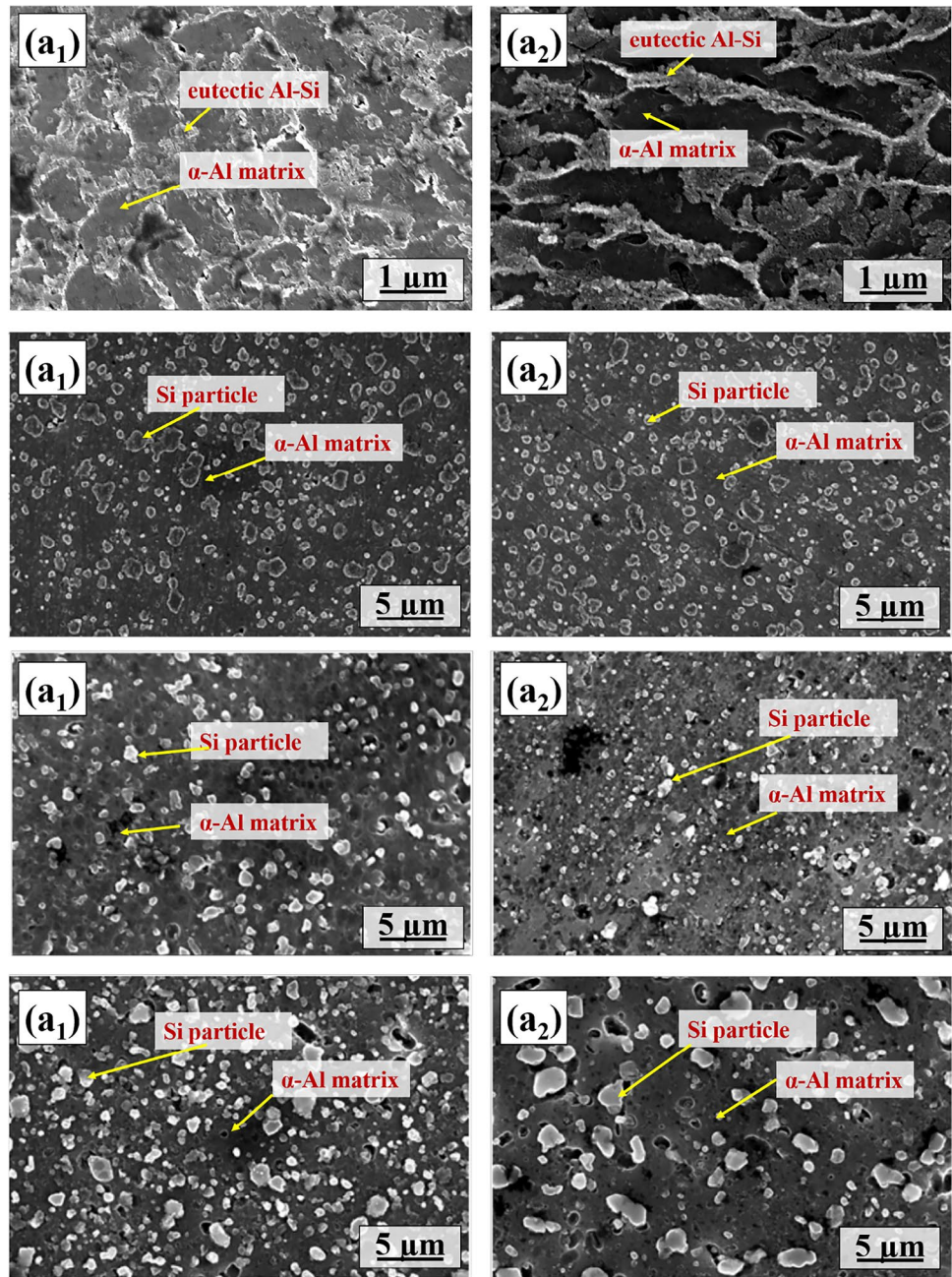


**Fig. 8** Spot EDS measurements and Si content distribution of horizontal section under different heat treatment conditions: **a** as-printed, **b** T6, **c** T2, and **d** T6-T2. **e** Comparison of Si content in Si particle and Al matrix

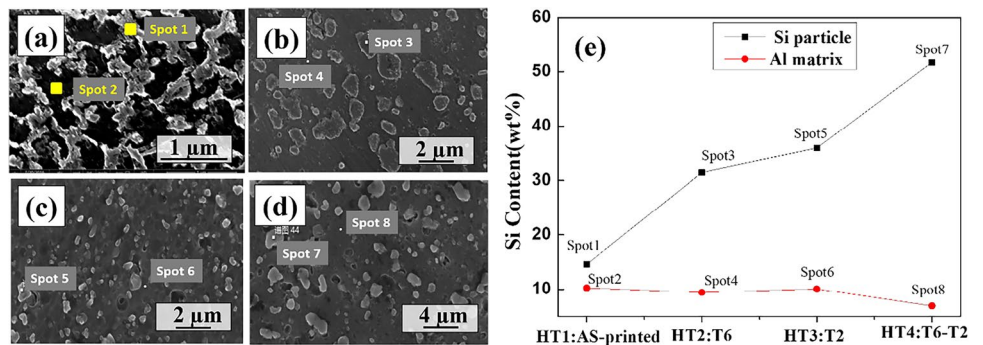




**Fig. 9** Tensile properties and residual stress of the LPB-Fed AlSi10Mg specimens under different conditions. **a** Ultimate tensile strength. **b** Yield strength. **c** Elongation. **d** Residual stress

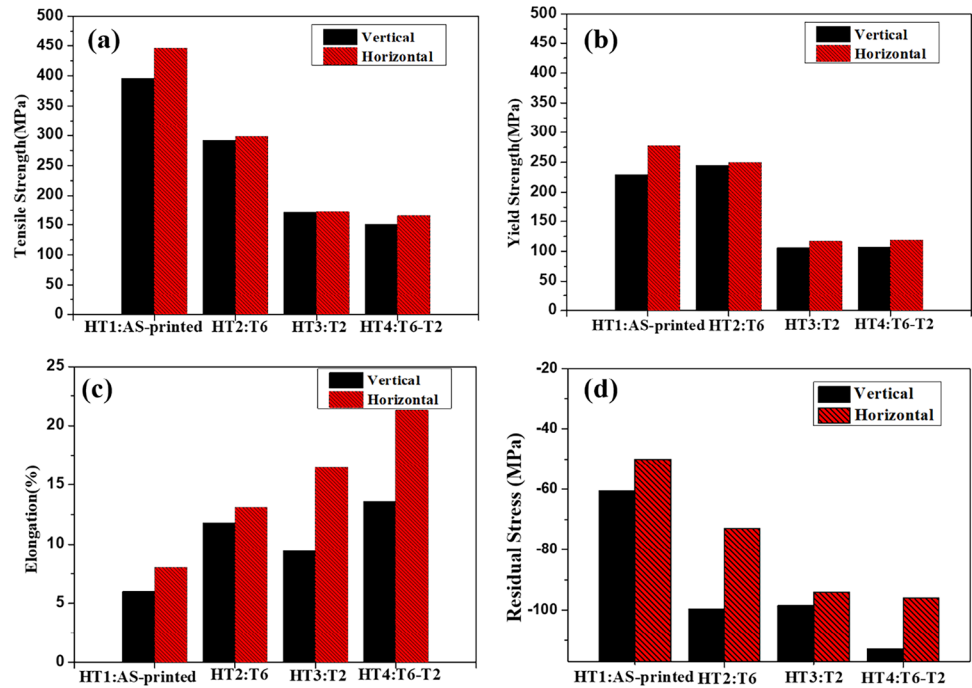


**Table 3** Tensile properties of the LPBFed AlSi10Mg specimens under different heat treatments

Heat treatment number	Tensile strength (MPa)		Yield strength (MPa)		Elongation (%)	
	Vertical	Horizontal	Vertical	Horizontal	Vertical	Horizontal
HT1	396	446	229	278	6	8
HT2	292	298	245	250	11.8	13.1
HT3	171.3	171.7	105.7	116.7	9.39	16.47
HT4	151	165	107.3	119	13.59	21.3

**Table 4** Residual stress of the LPBFed AlSi10Mg specimens under different heat treatments

Specimen number	Residual stress/ MPa			
	Point 1	Point 2	Point 3	Average
A-H	-77.46	-29.24	-49.35	-52.02
A-Z	-65.8	-55.13	-60.80	-60.58
B-H	-66.61	-81.77	-70.19	-72.86
B-Z	-99.42	-101.11	-98.30	-99.61
C-H	-123.87	-88.28	-70.03	-94.06
C-Z	-100.14	-98.18	-97.16	-98.49
D-H	-102.74	-87.91	-97.33	-95.99
D-Z	-138.83	-88.83	-110.83	-112.83

This suggests that the T6 treatment can not only eliminate anisotropy of the LPBFed AlSi10Mg specimens basically but also obtain a better combination of strength and plasticity. The residual stress of the LPBFed AlSi10Mg specimens under different heat treatments was presented in Table 4 and Fig. 9d. As suggested by results, the residual stress on the

surface of the LPBFed specimens after heat treatments was mainly compressive stress and higher than that of the as-printed specimens, indicating that heat treatments were good for the LPBFed parts. In addition, the vertical compressive stress was greater than horizontal compressive stress.

In order to understand the fracture mechanisms of the T6 treatment samples including “horizontal” and “vertical” ones, fracture morphology and EDS analysis of tensile specimens were carried out using SEM, as presented in Fig. 10. There was no defect on the tensile fracture of the vertical samples in Fig. 10a–c. Besides, the distribution of the dimples closely connected on the tensile fracture indicates that the fracture mode is mainly arbitrary fracture. Apart from that, the dispersed precipitation particles were found on the bottom of the dimples, which was favorable to increase the tensile properties.

The fracture morphology of horizontal specimens is shown in Fig. 10d–f, and obvious pores appeared on the tensile fracture. However, the dimples on the tensile fracture reveal that the fracture mode is dominated by the arbitrary fracture. Likewise, the bottom and side walls of the dimples

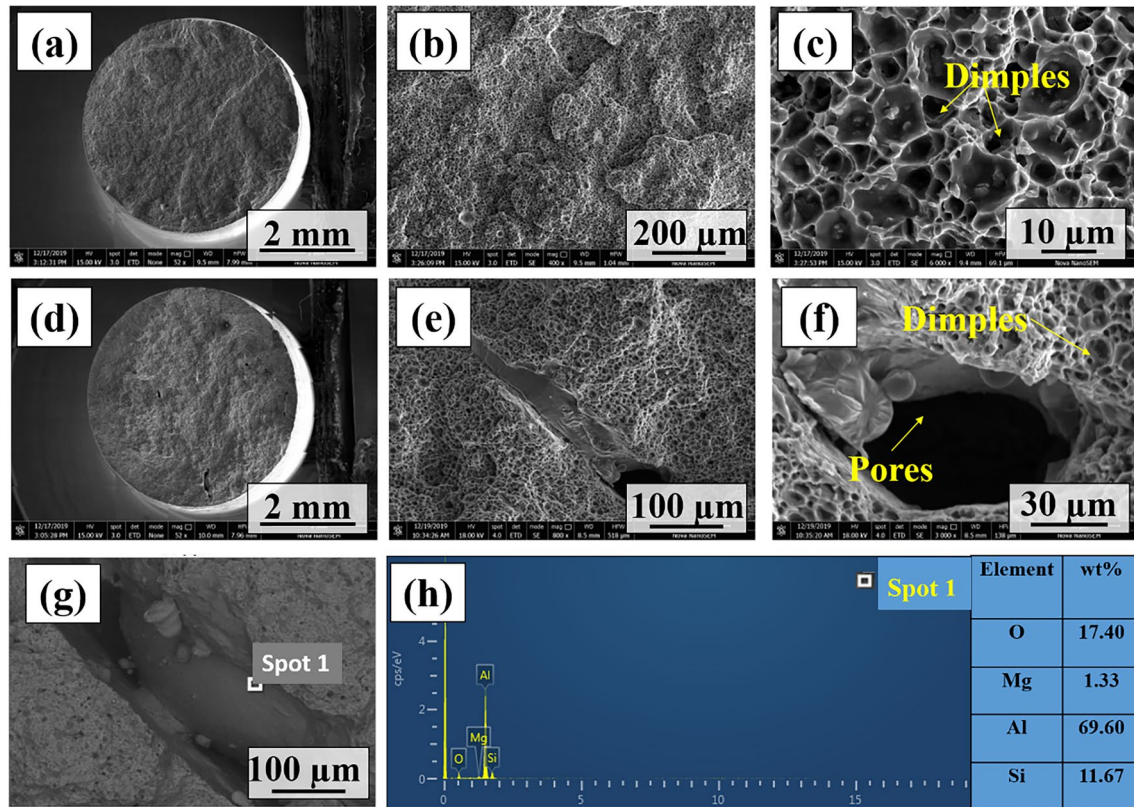


**Fig. 10** SEM images and EDS analysis of fractured surface profile of the LPBFed AlSi10Mg under HT2. **a–c** SEM images of fractured surface profile of the vertical sample. **d–f** SEM images of fractured surface profile of the horizontal sample. **g–h** EDS analysis of the horizontal sample

were dispersed by the enhanced precipitates. At the same time, the morphology of pores that appeared on the fracture was enlarged to investigate its mechanism. Besides, the inner wall of the pores was smooth, where there were irregular particles. The EDS analysis was performed on the inner wall of the pores to clarify its chemical composition in Fig. 10g–h. The oxygen content in this area reached 17.4% owing to the splash generated by the laser during the LPBF process. It is noteworthy that the splash produced is easy to fall on the formed part during the LPBF process of the horizontal specimens. The splash that partly melted together with the next powder layer may remain in the specimens, but this is related to the cross-sectional area of specimens. The larger the cross-sectional area is, the greater possibility of generating the pore defects caused by the splash is.

The kernel average misorientation (KAM) was analyzed according to EBSD results and performed in Fig. 11. The average value of KAM on vertical section (0.6916) was smaller than that of the horizontal section (0.75975) for the LPBFed AlSi10Mg samples, as shown in Fig. 11a. In general, a higher average value of KAM indicates a higher dislocation density, therefore, a

higher dislocation strengthening in the sample. Therefore, the strength and plasticity of the vertical section was smaller than that of the horizontal section for the LPBFed AlSi10Mg samples.

For the T6 treatment samples, as shown in Fig. 11b, the average values of KAM on vertical section (0.72425) and horizontal section (0.73675) were similar. For the T2 treatment samples, it can be observed from Fig. 11c that the average values of KAM on vertical section (0.66272) and horizontal section (0.66037) were similar. For the T6-T2 treatment samples, it can be observed from Fig. 11d that the average value of KAM on vertical section was 0.6637, while that on horizontal section was 0.78397. It can be found that there was a smallest difference in the average value of KAM between the vertical section and the horizontal section for the T6 samples, which was consistent with the difference of tensile strength and plasticity. That is to say, the T6 treatment weakens the direction difference to the greatest extent from dislocation strengthening and metal deformation mechanism. Besides, the average value of KAM for T2 heat treatment was the smallest, suggesting that the T2 treatment minimizes the stress concentration.

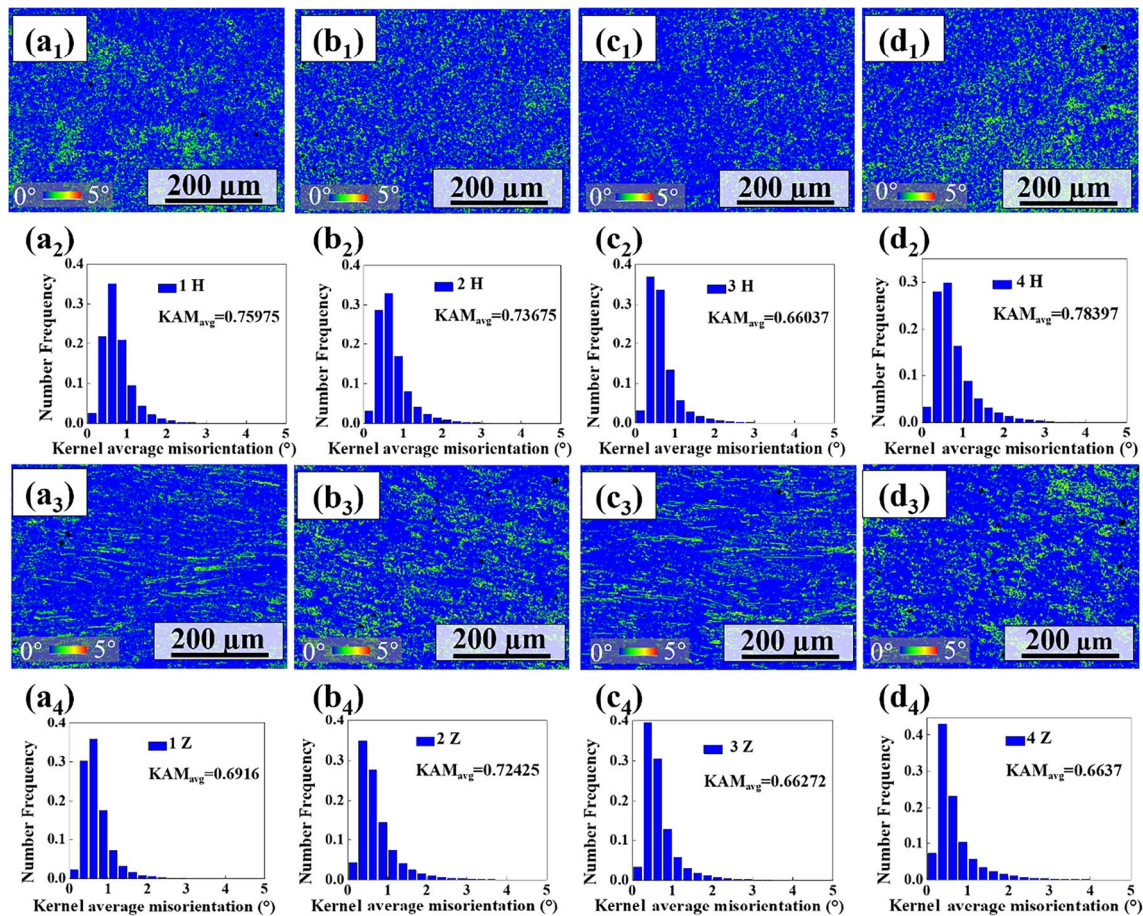


**Fig. 11** The kernel average misorientation (KAM) map on horizontal section, the histogram for KAM on horizontal section, the kernel average misorientation (KAM) map on vertical section, and the his-

togram for KAM on vertical section under different conditions. **a** As-printed. **b** T6 treatment. **c** T2 treatment. **d** T6-T2 treatment

## 4 Conclusions

The present work investigates the effect of heat treatment on microstructures and mechanical properties of AlSi10Mg alloy fabricated by LPBF. The key findings can be listed as follows:

(1) The obvious differences of microstructures for the LPBFed AlSi10Mg samples were attributed to the LPBF principle. For the “horizontal section,” the distribution of the melt pools was tightly arranged, which was consistent with the chessboard scanning. After the T6 and T6-T2 heat treatments, the proportion of equiaxed grains on the vertical section increased, which could explain the reduced anisotropy of the mechanical properties.

(2) The eutectic Al-Si phase for the LPBFed specimens was generated and distributed along the molten pool boundaries. After the heat treatments including T6, T2, and T6-T2, the eutectic Al-Si phase was transformed into Si particles uniformly distributed in  $\alpha$ -Al matrix. Nevertheless, the mass fraction of Si in the particles (%) and the

elongation (%) was the largest by T6-T2 treatment, while the tensile strength and yield strength were the smallest because of experiencing the whole process of “fully diffusion- nucleation-precipitation-growth.”

(3) For the LPBFed specimens, the mechanical properties of the horizontal direction were better than those of the vertical direction. Apart from that, the LPBFed AlSi10Mg samples at the vertical direction by the T6 treatment obtained the best combination of strength and plasticity, with a tensile strength of 292 MPa, a yield strength of 245 MPa, and a percentage elongation after the break of 11.8%. The dimples on the tensile fracture reveal that the fracture mode is dominated by arbitrary fracture.

(4) The relationship among the inverse pole figure (IPF) maps, pole figure (PF) maps, the mass fraction and distribution of Si in the Al matrix and Si particle, the grain size, kernel average misorientation (KAM), and mechanical properties under different heat treatments was established. The proportion of equiaxed grains on vertical section increased, which was favorable to reduce the anisotropy degree of the

mechanical properties. Moreover, the T6 treatment weakened the direction difference to the greatest extent from the distribution of KAM. Besides, the average value of KAM for T2 heat treatment was the smallest, indicating that the T2 treatment minimizes the stress concentration.

**Author contribution** XZ: supervising, editing, experiments. DD: supervising. AD: writing. QS: experiments. JS: experiments. LG: editing. BS: supervising, editing. ZC: experiments.

**Funding** This work was supported by the financial support of the National Key Research and Development Program of China grants (2022YFB4602300), the National Natural Science Foundation of China (nos. 51901135, 52071205), and Equipment Pre-research Shared Technology Project of China (50922060201).

**Data availability** Not applicable

**Code availability** Not applicable

## Declarations

**Ethics approval** Not applicable

**Consent to participate** The authors declare that they consent to participate in this paper.

**Consent for publication** The authors declare that they consent to publish this paper.

**Conflict of interest** The authors declare no competing interests.

**Disclaimer** The State Key Labs of Advanced High-temperature Materials and Precision Forming and Metal Matrix Composites do not mind being the author's unit. They also do not affect your decision to publish and share the results in your journal.

## References

- Laguna O, Lietor P, Iglesias Godino F, Corpas-Iglesias F (2021) A review on additive manufacturing and materials for catalytic applications: milestones, key concepts, advances and perspectives. *Mater Design* 208:109927. <https://doi.org/10.1016/j.matdes.2021.109927>
- Blakey-Milner B, Gradl P, Snedden G, Brooks M, Pitot J, Lopez E, Leary M, Berto F, Plessis A (2021) Metal additive manufacturing in aerospace: a review. *Mater Design* 209:110008. <https://doi.org/10.1016/j.matdes.2021.110008>
- Zhang J, Song B, Wei Q, Bourell D, Shi Y (2019) A review of selective laser melting of aluminum alloys: processing, microstructure, property and developing trends. *J Mater Sci Technol* 35:270–284. <https://doi.org/10.1016/j.jmst.2018.09.004>
- Singh R, Gupta A, Tripathi O, Srivastava S, Singh B, Awasthi A, Rajput S, Sonia P, Singhal P, Saxena K (2020) Powder bed fusion process in additive manufacturing: an overview. *Mater Today: Proceedings* 26:3058–3070. <https://doi.org/10.1016/j.matpr.2020.02.635>
- Wang L, Jiang X, Zhu Y, Zhu X, Sun J, Yan B (2018) An approach to predict the residual stress and distortion during the selective laser melting of AlSi10Mg parts. *Int J Adv Manuf Tech* 97:3535–3546. <https://doi.org/10.1007/s00170-018-2207-3>
- Calignano F, Cattano G, Manfredi D (2018) Manufacturing of thin wall structures in AlSi10Mg alloy by laser powder bed fusion through process parameters. *J Mater Process Tech* 255:773–783. <https://doi.org/10.1016/j.jmatprotec.2018.01.029>
- Yang T, Liu T, Liao W (2019) The influence of process parameters on vertical surface roughness of the AlSi10Mg parts fabricated by selective laser melting. *J Mater Process Tech* 266:26–36. <https://doi.org/10.1016/j.jmatprotec.2018.10.015>
- Shen X, Cheng Z, Wang C, Wu H, Yang Q, Wang G, Huang S (2021) Effect of heat treatments on the microstructure and mechanical properties of Al-Mg-Sc-Zr alloy fabricated by selective laser melting. *Opt Laser Technol* 143:107312. <https://doi.org/10.1016/j.optlastec.2021.107312>
- Wang Y, Lin X, Kang N, Wang Z, Liu Y, Huang W (2022) Influence of post-heat treatment on the microstructure and mechanical properties of Al-Cu-Mg-Zr alloy manufactured by selective laser melting. *J Mater Sci Technol* 111(3):5–48. <https://doi.org/10.1016/j.jmst.2021.09.036>
- Babu A, Huang A, Birbilis N (2021) On the heat treatment and mechanical properties of a high solute Al-Zn-Mg alloy processed through laser powder bed fusion process. *Mat Sci Eng A* 807:140857. <https://doi.org/10.1016/j.msea.2021.140857>
- Xiao Y, Yang Q, Bian Z, Chen H, Wu Y, Lian Q, Chen Z, Wang W (2021) Microstructure, heat treatment and mechanical properties of TiB<sub>2</sub>/Al-7Si-Cu-Mg alloy fabricated by selective laser melting. *Mat Sci Eng A* 809:140951. <https://doi.org/10.1016/j.msea.2021.140951>
- Prashanth K, Scudino S, Klauss H, Surreddi K, Löber L, Wang Z, Chaubey A, Kühn U, Eckert J (2014) Microstructure and mechanical properties of Al-12Si produced by selective laser melting: effect of heat treatment. *Mat Sci Eng A* 590:153–160. <https://doi.org/10.1016/j.msea.2013.10.023>
- Li X, Wang X, Saunders M, Suvorova A, Zhang L, Liu Y, Fang M, Huang Z, Sercombe T (2015) A selective laser melting and solution heat treatment refined Al-12Si alloy with a controllable ultrafine eutectic microstructure and 25% tensile ductility. *Acta Mater* 95:74–82. <https://doi.org/10.1016/j.actamat.2015.05.017>
- Wang P, Li H, Prashanth K, Eckert J, Scudino S (2017) Selective laser melting of Al-Zn-Mg-Cu: heat treatment, microstructure and mechanical properties. *J Alloy Compd* 707:287–290. <https://doi.org/10.1016/j.jallcom.2016.11.210>
- Kang N, Coddet P, Ammar M-R, Liao H, Coddet C (2017) Characterization of the microstructure of a selective laser melting processed Al-50Si alloy: effect of heat treatments. *Mater Charact* 130:243–249. <https://doi.org/10.1016/j.matchar.2017.06.026>
- Wang P, Gammer C, Brenne F, Niendorf T, Eckert J, Scudino S (2018) A heat treatable TiB<sub>2</sub>/Al-3.5Cu-1.5Mg-1Si composite fabricated by selective laser melting: microstructure, heat treatment and mechanical properties. *Compos Part B* 147:162–168. <https://doi.org/10.1016/j.compositesb.2018.04.026>
- Zhang M, Zhou X, Wang D, Zhu W, Li J, Zhao Y (2019) AlCo-CuFeNi high-entropy alloy with tailored microstructure and outstanding compressive properties fabricated via selective laser melting with heat treatment. *Mat Sci Eng A* 743:773–784. <https://doi.org/10.1016/j.msea.2018.11.118>
- Zhang H, Gu D, Dai D, Ma C, Li Y, Cao M, Li S (2020) Influence of heat treatment on corrosion behavior of rare earth element Sc modified Al-Mg alloy processed by selective laser melting. *Appl Surf Sci* 509:145330. <https://doi.org/10.1016/j.apsusc.2020.145330>
- Wang C, Zhu J, Wang G, Qin Y, Sun M, Yang J, Shen X, Huang S (2022) Effect of building orientation and heat treatment on the anisotropic tensile properties of AlSi10Mg fabricated by

- selective laser melting. *J Alloy Compd* 895:162665. <https://doi.org/10.1016/j.jallcom.2021.162665>
20. Wei P, Chen Z, Zhang S, Fang X, Lu B, Zhang L, Wei Z (2021) Microstructure, Effect of T6 heat treatment on the surface tribological and corrosion properties of AlSi10Mg samples produced by selective laser melting. *Mater Charact* 171:110769. <https://doi.org/10.1016/j.matchar.2020.110769>
21. Li W, Li S, Liu J, Zhang A, Zhou Y, Wei Q, Yan C, Shi Y (2016) Effect of heat treatment on AlSi10Mg alloy fabricated by selective laser melting: microstructure evolution, mechanical properties and fracture mechanism. *Mat Sci Eng A* 663:116–125. <https://doi.org/10.1016/j.msea.2016.03.088>
22. Takata N, Kodaira H, Sekizawa K, Suzuki A, Kobashi M (2017) Change in microstructure of selectively laser melted AlSi10Mg alloy with heat treatments. *Mat Sci Eng A* 704:218–228. <https://doi.org/10.1016/j.msea.2017.08.029>
23. Subramaniyan A, Reddy A, Mathias S, Shrivastava A, Raghupatruni P (2021) Influence of post-processing techniques on the microstructure, properties and surface integrity of Al-Si-Mg alloy processed by laser powder bed fusion technique. *Surf Coat Tech* 425:127679. <https://doi.org/10.1016/j.surfcoat.2021.127679>
24. Butler C, Babu S, Lundy R, Meehan R, Punch J, Jeffers N (2021) Effects of processing parameters and heat treatment on thermal conductivity of additively manufactured AlSi10Mg by selective laser melting. *Mater Charact* 173:110945. <https://doi.org/10.1016/j.matchar.2021.110945>
25. Guo Y, Su H, Zhou H, Shen Z, Liu Y, Zhang J, Liu L, Fu H (2022) Unique strength-ductility balance of AlCoCrFeNi<sub>2,1</sub> eutectic high entropy alloy with ultra-fine duplex microstructure prepared by selective laser melting. *J Mater Sci Technol* 111:298–306. <https://doi.org/10.1016/j.jmst.2021.10.013>
26. Wang L, Zhang Y, Hua X, Shen C, Li F, Huang Y, Ding Y, Zhang P, Lu Q, Zhang T, Shang J (2021) Twin-wire plasma arc additive manufacturing of the Ti–45Al titanium aluminide: processing, microstructures and mechanical properties. *Intermetallics* 136:107277. <https://doi.org/10.1016/j.intermet.2021.107277>
27. Sridharan N, Gussev M, Seibert R, Parish C, Norfolk M, Terrani K, Babu S (2016) Rationalization of anisotropic mechanical properties of Al-6061 fabricated using ultrasonic additive manufacturing. *Acta Mater* 117:228–237. <https://doi.org/10.1016/j.actamat.2016.06.048>
28. Rao J, Zhang Y, Fang X, Chen Y, Wu X, Davies C (2017) The origins for tensile properties of selective laser melted aluminium alloy A357. *Addit Manuf* 17:113–122. <https://doi.org/10.1016/j.addma.2017.08.007>
29. Han Q, Jiao Y (2019) Effect of heat treatment and laser surface remelting on AlSi10Mg alloy fabricated by selective laser melting. *Int J Adv Manuf Tech* 102:3315–3324. <https://doi.org/10.1007/s00170-018-03272-y>

**Publisher's note** Springer Nature remains neutral with regard to jurisdictional claims in published maps and institutional affiliations.

Springer Nature or its licensor (e.g. a society or other partner) holds exclusive rights to this article under a publishing agreement with the author(s) or other rightsholder(s); author self-archiving of the accepted manuscript version of this article is solely governed by the terms of such publishing agreement and applicable law.